Effects from the Target Plate Geometry on Fluctuations of Helium Plasma in the Linear Divertor Simulator Magnum-PSI

Masayuki YOSHIKAWA, Hirohiko TANAKA[1)], Yuki HAYASHI[2)], Shin KAJITA[3)],
Hennie van der MEIDEN[4)], Jordy VERNIMMEN[4)], Thomas MORGAN[4)], Junko KOHAGURA,
Yoriko SHIMA, Satoshi TOGO, Naomichi EZUMI, Yousuke NAKASHIMA
and Mizuki SAKAMOTO

Plasma Research Center, University of Tsukuba, Tsukuba 305-8577, Japan
[1)]Graduate School of Engineering, Nagoya University, Nagoya 464-8603, Japan
[2)]National Institute for Fusion Science, National Institutes of Natural Sciences, Toki 509-5292, Japan
[3)]Graduate School of Frontier Sciences, University of Tokyo, Kashiwa 277-8561, Japan
[4)]DIFFER-Dutch Institute for Fundamental Energy Research, 5612 AJ Eindhoven, The Netherlands

(Received 1 May 2022 / Accepted 21 August 2022)

With the help of the linear divertor simulation device Magnum-PSI, a fluctuation investigation of the impact of the target plate geometry was conducted. We simultaneously quantify coherent low-frequency fluctuations with a newly built 70-GHz microwave reflectometry system, a reciprocating probe, a light emission detector system, and a fast-framing camera system. The strong low-frequency fluctuations were observed at both the electron density and the plasma radiations by moving the target plate along the magnetic field line. Furthermore, a strong peak in fluctuation intensity and the influence of the target plate tilt angle on the fluctuation intensity were noted.

Keywords: fluctuation, divertor simulator, Magnum-PSI

DOI: 10.1585/pfr.17.1402100

1. Introduction

One of the most important issues in nuclear fusion reactors is the investigation of the mechanisms of detached plasmas in divertor plasmas [1]. The temperature and heat flux of hot plasma from the core region to the scrape-off layer (SOL) decrease along the magnetic field to the diverter plate under detached plasma conditions. The radiation zone, ionization region, recombination region, and momentum loss region are thought to make up the plasma conditions along the magnetic field to the diverter plate [1–4]. In addition, in some linear plasma simulators, including NAGDIS-II, Pilot-PSI, and Magnum-PSI [5–15], and the SOL of the tokamak plasma of ASDEX Upgrade [16], low-frequency fluctuations around the recombination front region have been observed in the detached plasma conditions. These fluctuations result in radial particle losses across the magnetic field.

In the divertor studies, the characteristics of fluctuations along with the magnetic field line to the divertor plate have not been thoroughly explored. In this study, we conducted electrostatic fluctuation measurements on the target plate and examined them using microwave reflectometry and a reciprocating Langmuir probe fitted in Magnum-PSI, which can achieve the SOL magnetic field conditions that are crucial to ITER. Furthermore, direct plasma visible radiation was measured at the same axial position as the Thomson scattering (TS) system observation port using a photodiode emission measurement device and a fast-framing camera, respectively. In addition, data with a high-time resolution were simultaneously obtained by the Langmuir probes installed on the fast reciprocating probe system.

Stronger oscillations in the ionization zone and/or recombination front region were observed in hydrogen plasmas in Pilot-PSI in earlier studies of linear divertor plasmas [6, 7]. In an area that was axially localized and where pure He plasmas in NAGDIS-II experienced high volume recombination, the cross-field transport was enhanced [9–11]. The cross-field transport appeared to be enhanced in the region between the TS axial location and the target plate (Z_{tgt} = 200 mm) at 1.4 Pa gas pressure [15]. In Magnum-PSI, it was discovered that the cross-field transport took place right in front of the target plate [15]. It is still unknown how the target plate geometry affects the fluctuations in the detached plasma. To examine the spatial distribution of the fluctuations and the effects of the plasma injection angle on the target plate, we performed a fluctuation analysis in this study by varying the target plate position from the axial position of the TS system measurement and the target plate tilt angle.

---

author's e-mail: yosikawa@prc.tsukuba.ac.jp

2. Experimental Apparatus

Magnum-PSI, a linear superconducting device can replicate divertor plasmas relevant to ITER with high ion fluxes up to 10^{25} $\mathrm{m^{-2}s^{-1}}$ in the presence of a strong magnetic field [17, 18]. In the magnetic field, up to $B = 2.5$ T, a cascaded arc discharge generates an electron density of $n_e \sim 10^{19}$ - 10^{21} $\mathrm{m^{-3}}$ and an electron temperature of $T_e \sim$ 1 - 5 eV. The vacuum vessel is split into three pieces by a differential pumping system that consists of two orifice plates (skimmers) and root pumps. Under similar source plasma circumstances, this design enables the detached plasma condition in the downstream region of the vacuum vessel (target chamber). Schematics of this experimental setup are shown in Fig. 1 and include: (a) the measurement system setup at the TS axial position, (b) a schematic cross-sectional view of the vacuum vessel, and (c) the fast reciprocating probe head. The magnetic field was set as the Z-axis. A YAG-TS system is fitted in the target chamber to obtain the temperature and electron density radial profiles [19] at $Z = 0$ mm. A single-position spectroscopy system (Avantes, AvaSpec-2048-USM2-RM) measures the line-integrated emissions from the plasma over the wavelength range of 299 - 950 nm at the same axial position as the TS system [20]. A 70-GHz microwave reflectometry system was positioned at the same axial position as the TS system to measure high-time resolution signals. At the same axial position as the TS, the photodiode system uses the TS system's optical collection system to measure the line-integrated plasma radiation. Additionally, a Langmuir probe device mounted on a reciprocating arm and producing a high-spatiotemporal-resolution signal was employed [13–15]. In addition, a fast-framing camera that could see a larger region around the probe head was put in the same location as the TS system. The following information is supplied regarding various fluctuation measurement systems.

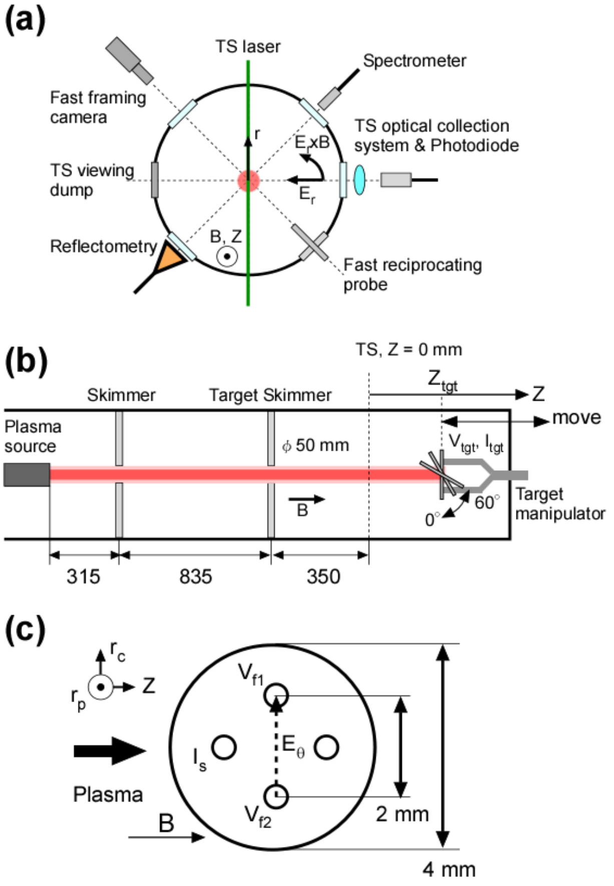

Fig. 1 Diagrams of (a) the measurement system setup at the Thomson scattering (TS) axial position, (b) a schematic cross-sectional view of the vacuum vessel, and (c) fast reciprocating probe head.

2.1 Microwave reflectometry system

The frequency multiplier-containing microwave reflectometry system (Fig. 2), which was built as the interferometer system in GAMMA 10 [6–8, 12], was situated 350 mm ($Z = 0$ mm) downstream from the target skimmer. It is a heterodyne reflectometry system equipped with a 17.5-GHz phase-locked dielectric resonator oscillator, a 37.5-MHz temperature-compensated crystal oscillator, and frequency multipliers for obtaining both 70-GHz probing beam and reference beam. A horn antenna is set perpendicular to the plasma beam at the downside port. The cutoff plasma density of the system was 6×10^{19} $\mathrm{m^{-3}}$. The system has the capability of measuring density fluctuations at the cutoff layer. Phase detection signals are recorded by a high-speed data acquisition system with a sampling rate of 1 MSa/s.

2.2 Photodiode measurement system

Molecular activated recombination and ion-electron recombination are effective production channels for exciting neutrals under the diverter simulation experimental condition [20]. The light emission fluctuation could depend on both the electron and He ion fluctuations. Without using any optical filters, the photodiode's visible emission detector (Thorlabs, SM1PD1A) was utilized to look into this. The photodiode was connected to one of the optical fibers of the TS system's optical collection system. Using the high-speed data acquisition system (PXI, 1 MSa/s, 8 bit), the photodiode's output signal was also captured.

2.3 Fast-framing camera

To capture a large spatial region of the plasma, a fast-framing camera (Phantom V12, 12-bit grayscale, 997 kfps, 256 px × 128 px) was set up. Without using an optical filter, the line-integrated visible light emission perpendicular to the magnetic field was obtained. Z represents the axial displacement along the magnetic field direction from the TS axial location. We chose a camera frame rate and exposure duration for this experiment of 97,073 fps and 3 μs, respectively. The pixel resolution was ~0.36 mm/px, and

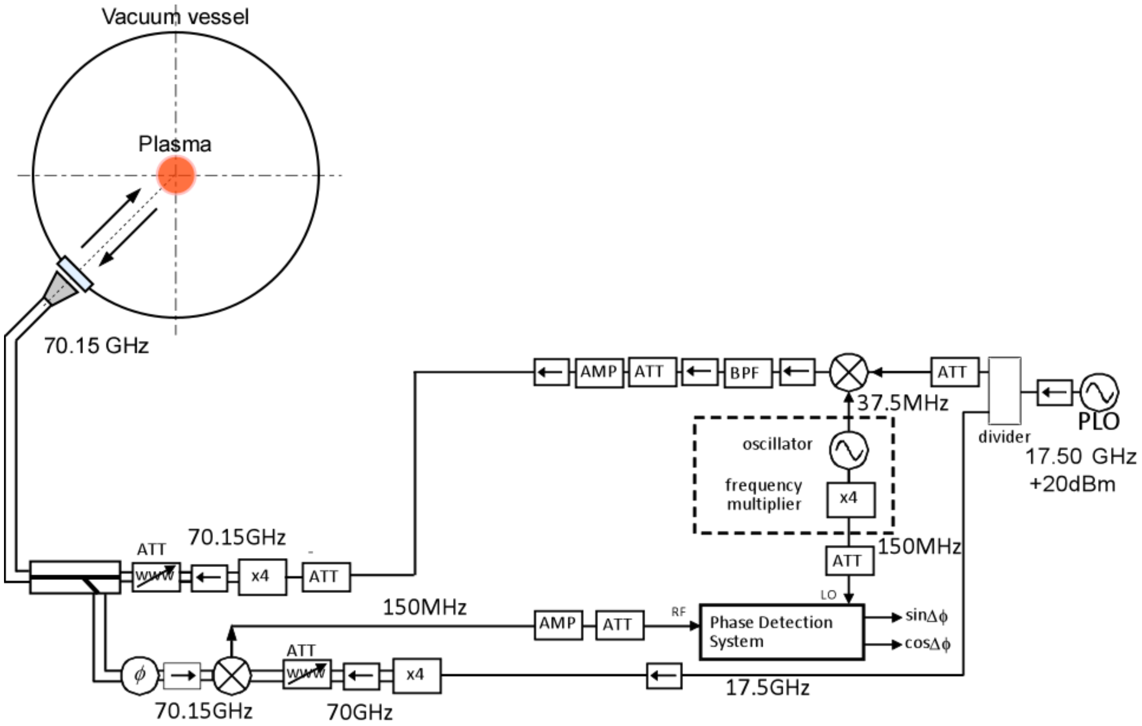

Fig. 2 System diagram for 70-GHz microwave reflectometry.

the frame size was 128 px × 256 px. For each plasma shot, 20,000 frames were captured.

2.4 Target plate

The target plate is a lengthy target manipulator system that installs various target forms. As shown in Fig. 1 (b), the target plate facing the main plasma in this study was positioned at $Z = 50$, 100, 150, 200, and 300 mm behind the TS axial position. When the target plate location was Z, we set the measurement condition to Z_{tgt}. The target plate was fitted with the rectangular carbon plate (50 mm × 100 mm), whose tilt angle (A) could be adjusted to 0°, 30°, and 60° perpendicular to the magnetic field. The target plate in this study was on the floating potential (V_{tgt}).

2.5 Fast reciprocating probe

The reciprocating Langmuir probe was set at $Z = 0$ mm. For Pilot-PSI and Magnum-PSI, specifics of the reciprocation system have already been documented [13–15]. A schematic of the probe head with several electrodes is shown in Fig. 1 (c). Four tungsten electrodes with a combined diameter of 0.5 mm and an exposed length of 0.5 mm made up the probe head, which was constructed from a ceramic shaft with a diameter of 4 mm. In this study, three of the electrodes were used for an electrode for measuring the ion saturation current (I_{s}) with biased at −100 V and two for floating potentials (V_{f1} and V_{f2}). To measure the azimuthal electric field (E_θ), the two electrodes for V_{f1} and V_{f2} were placed 2 mm apart perpendicular to the magnetic field. The following was calculated as the midpoint floating potential: $V_{\mathrm{f}} = (V_{\mathrm{f1}} + V_{\mathrm{f2}})/2$. Utilizing separate analog-to-digital converters (Yokogawa 720254, 500 kSa/s, 16 bits), these signals were simultaneously captured. The probe head was moved by compressed air from the radius of $r = -50$ mm to the radial center of $r = 0$ mm during the plasma discharge. Measurements at $r = 0$ mm were taken for a short while before the probe head was extracted. A small camera was used to record the reciprocation of the probe, and a mark sensor that read barcodes every 1 mm was used to measure the probe's position. The speeds for insertion and extraction were roughly 200 - 300 mm/s.

3. Fluctuation Measurement Experiments in Magnum-PSI

3.1 Experimental setup

Pure He plasma was produced under the magnetic field strength of 0.6 T, and the discharge current of the plasma source was 140 A. The plasma duration was approximately 5 - 6 s. In the target chamber, the background pressure ranged from 3.1~3.4 Pa. At the target plate position of $Z_{\mathrm{tgt}} = 150$ mm, the electron (a) temperature and (b) density radial profiles recorded with the TS system are displayed in Fig. 3. The cutoff density for the 70 GHz reflectometry system is also shown in Fig. 3 (b). Around −10 mm of the reflectometry system's probing beam is reflected. The electron temperature is 0.48 eV, and the density is $2.7 \times 10^{20}\ \mathrm{m}^{-3}$. Figure 4 shows the electron temperatures and densities of Z_{tgt} dependence obtained by the

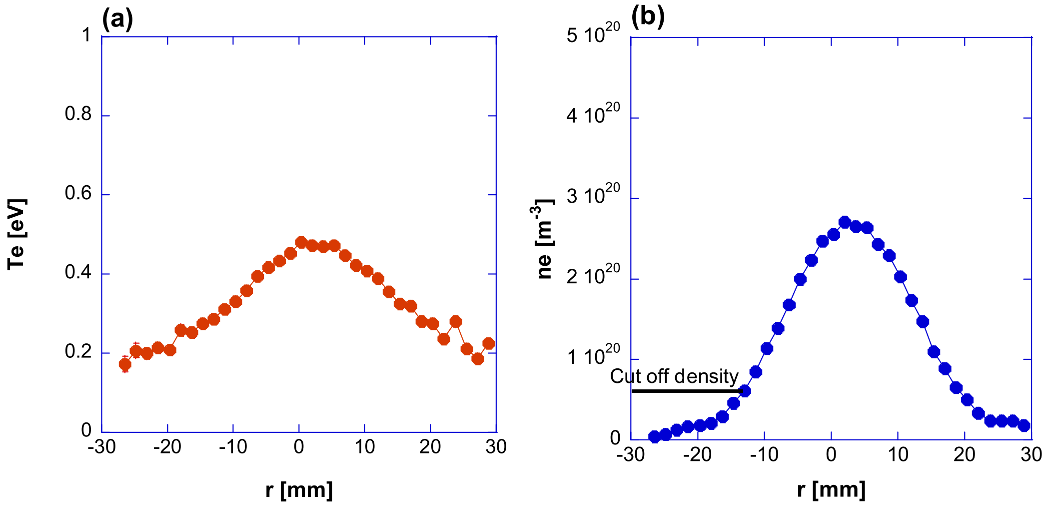

Fig. 3 Electron (a) temperature and (b) density radial profiles. The microwave reflectometry system's cut off density is also displayed in Fig. 3 (b).

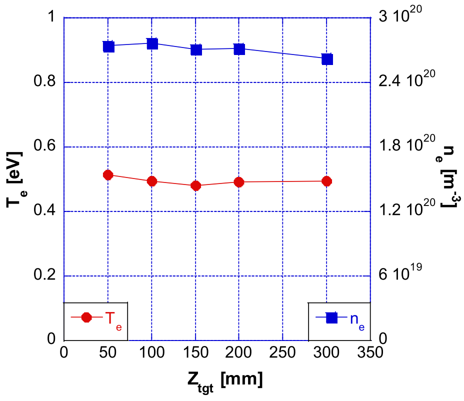

Fig. 4 Electron temperature and density Z_{tgt} dependences.

TS system by changing the target plate position shot-by-shot. Concerning Z_{tgt}'s position, they are both essentially constant. The radial profiles of electron density and temperature were unaffected by fluctuations in target plate tilt angle.

3.2 Fluctuation measurements with changing target plate position

The fluctuations of electron density, visible emission, and ion saturation current are measured by the reflectometry system, the fast-framing camera, the fast reciprocating probe, and the photodiode measurement system, by changing the target plate position and its tilt angle, shot-by-shot. Figure 5 displays, respectively, the output of the reflectometry system (a) and the line-integrated visible radiation measurement system (b), at the same axial position as the TS system with a target plate position of $Z_{\mathrm{tgt}} = 150$ mm, and the target plate tilt angle of $A = 0°$. The distinct drops at $t = 3$ - 4 s and 5 - 6 s seen in Fig. 5 (b) represent, respectively, the impact of the fast reciprocating probe and the termination of the plasma discharge. In Fig. 6, blue, red, and orange lines and their corresponding dotted lines, respectively, at the target plate position of $Z_{\mathrm{tgt}} = 150$ mm, represent the FFT-analyzed spectra of the plasma emission (PD), target plate potential (V_{tgt}), and electron density (n_{e}) measured by the reflectometry system both during and after the plasma. Except for the target plate, the spectra all show the same strong coherent low-frequency fluctuations between 3.4 and 6.8 kHz. Figures 7 (a) - (c) show a fast camera image at $t = 3.0$ s; a two-dimensional (2D) image of the fluctuation power spectral density at the fluctuation frequency of 3.4 kHz shown as a contour plot; and the power spectrum of the fluctuation at the pixel position of $(x, z) = (125, 64)$, respectively. FFT analysis was used to calculate the 2D images of the fluctuation intensity and phase angle concerning the temporal evolution of each 5 px × 5 px-averaged intensity of plasma emission. The left and right sides stand for the plasma upstream and downstream from the plasma source, respectively. At the upstream, the core plasma diameter is approximately 100 px and 5 cm. Using the fast-framing camera, the 3.4 kHz low-frequency fluctuation could be seen clearly. While the helium emission measurements, PD in Fig. 6 and Fig. 7 (c), measure the helium emission of the line-of-sight of the plasma, they get the broad frequency fluctuations at around 30 kHz. The differences between them are the larger power at 3.4 kHz and the smaller power at 30 kHz in Fig. 7 (c) than in Fig. 6. The higher frequency fluctuations occurred in the plasma center because of the absence of it the n_{e} fluctuation in Fig. 6.

Figure 8 shows (a) the spectrum obtained using the spectrometer system and (b) the Z_{tgt} dependences of the highly excited states of helium line emission intensities for wavelengths of 355.4 nm (2^3P–10^3D), 358.7 nm (2^3P–9^3D), and 363.4 nm (2^3P–8^3D). The recombined helium spectra from the more highly excited states and the con-

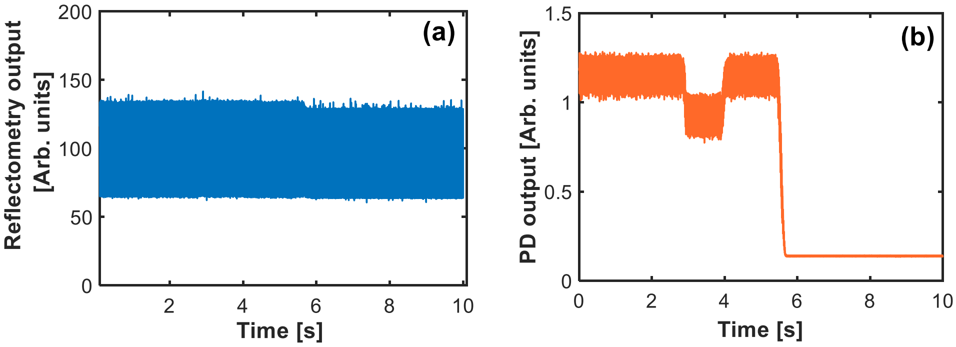

Fig. 5 (a) Reflectometry system output; (b) Output from a photodiode emission detector.

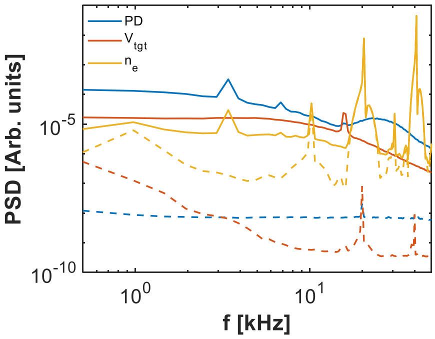

Fig. 6 The FFT analyzed spectra of the photodiode output (blue), target plate potential (red), and electron density fluctuation (orange). The solid and dotted lines represent the power spectral densities during and after the plasma, respectively.

tinuum radiation with a wavelength of 320 - 343 nm have been observed, according to plasma spectroscopy. Decreases in the emission intensities of every emission line are observed near $Z_{tgt} = 50$ mm. The spectrometer system's output spectra almost exactly match the helium atom line emissions in all Z_{tgt} locations. Unfortunately, data at the target plate position $Z_{tgt} > 150$ mm were not obtained because of the trigger error of the spectroscopy system; however, it was believed that the He line emissions' intensities had grown from $Z_{tgt} = 50$ to $Z_{tgt} = 100$ mm and kept almost constant from $Z_{tgt} > 100$ mm, axial profiles and the electron densities and temperatures almost remained constant due to the intensities of images acquired by the fast-framing camera.

At the target plate position of $Z_{tgt} = 150$ mm, the fast reciprocating probe was used to determine the radial profiles of the ion saturation current (I_s) and floating potentials (V_{f1} and V_{f2}) shown in Fig. 9.

Additionally, Fig. 10 displays the plasma center's ion saturation current in opposition to Z_{tgt} as well as the floating potential, $V_f = (V_{f1} + V_{f2})/2$. V_f and I_s remained roughly constant along the Z_{tgt}, within the margin of error. The coherent fluctuation intensities of the electron density and plasma emissions, which were obtained by the fast-framing camera of axial dependences against the Z_{tgt} location at a frequency of approximately 2.5 - 5.5 kHz, are shown in Fig. 11. The electron density and emission fluctuations are almost similar along the Z_{tgt} position. At $Z_{tgt} = 150$ mm, the electron density and plasma emission both exhibit distinct fluctuation intensity peaks.

3.3 Tilt angle dependence of fluctuation

When the tilt angle was adjusted from 0° to 60°, as well as the position of the target plate, the electron temperatures and densities were nearly identical with a 5% inaccuracy. In these plasma circumstances, the target plate tilt angle had little to no impact on the temperatures and densities of the electrons. At $Z_{tgt} = 150$ mm and $A = 0°$, the fluctuation frequencies of 3.4 and 6.8 kHz were seen, as shown in Figs. 6 and 7 (c). Figure 12 shows the fluctuation intensities of the electron density at a frequency around 2.5 - 5.5 kHz when the target plate tilt angle was changed against the target plate position. As compared to $A = 30°$ and 60°, the target plate tilt angle at 0° has substantially higher fluctuation intensities.

4. Discussion

The He plasmas' electron temperatures and densities measured at $B = 0.6$ T were around 0.2 - 0.5 eV and 1 - 3 × 10^{20} m^{-3}, respectively. With the aid of reflectometry, photodiode measurement, and a fast-framing camera, low-frequency coherent fluctuations in electron density and plasma radiation were discovered. At $Z_{tgt} = 150$ mm, the reflectometry was used to measure the radial positions of approximately $r \sim 0.01$ m. The reflectometry, photodiode, and high-speed camera all recorded peak fluctuation frequencies of about 3.4 kHz. By assuming $T_e = T_i$ [9, 10], the plasma potential could be derived using: $V_p \sim V_f + 3.7T_e$ and the radial electric field strength ($E_r = -dV_p/dr$) was determined. The radial profile of the electric field strength E_r at $Z_{tgt} = 150$ mm is shown in Fig. 13. As Z_{tgt} rises, the E_r strengths at $r \sim -20$ mm rise as well (Fig. 14). E_r at $Z_{tgt} = 150$ mm is approximately 0.25 kV/m at the plasma radius of ~ -20 mm. The plasma rotation affects the fluctuation that is being noticed. The ro-

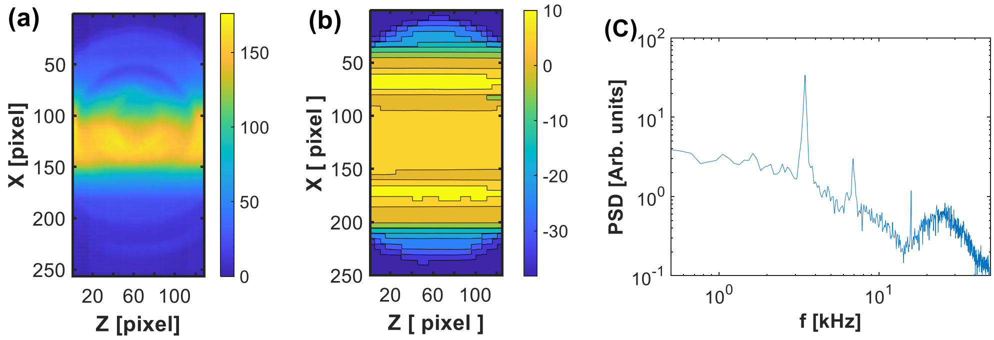

Fig. 7 (a) Fast-framing camera image at $t = 3.0$ s; (b) 2D image of fluctuation intensity at 3.4 kHz; (c) fluctuation power spectrum at the pixel position of $(x, z) = (125, 64)$.

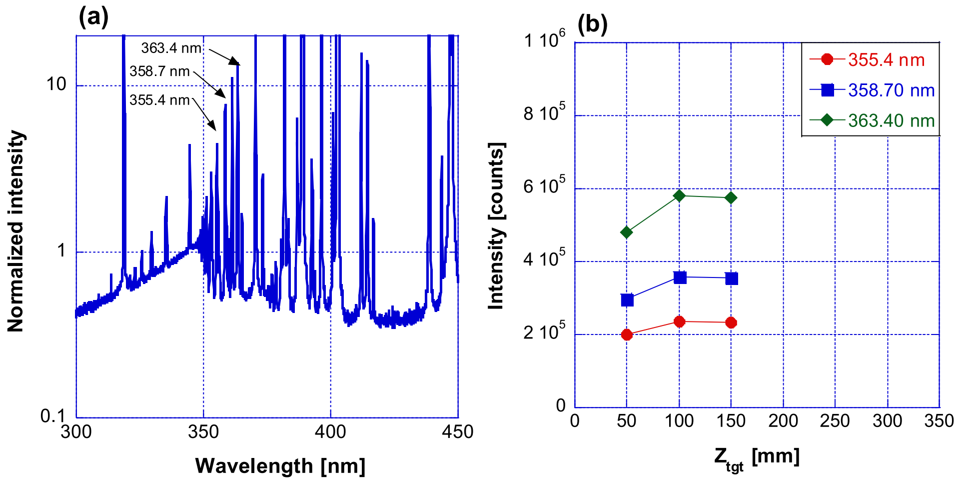

Fig. 8 (a) Emission spectrum at $Z_{\mathrm{tgt}} = 150$ mm and (b) Z_{tgt} dependences of the He line emissions measured using the spectrometer.

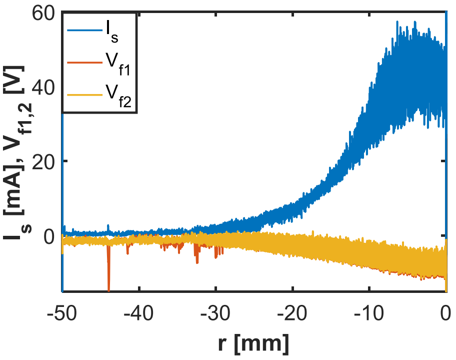

Fig. 9 Ion saturation current (I_s, blue line) and floating potential radial (V_{f1}, red line; V_{f2}, orange line) profiles measured using the fast reciprocating probe.

tational speed of the $E \times B$ drift was $v_\theta = E_r/B$, which was ~0.4 km/s. The fluctuation frequency was $f_\theta = v_\theta/(2\pi r)$ which was 3.4 kHz, and the mode number was $m = 1$, which may be equivalent to the same rotational speed at $r \sim -20$ mm (Fig. 15). The I_s radial profile's fluctuation spectrogram is shown in Fig. 16. Although it is feeble, the coherent fluctuation at 3.4 kHz can be seen at $r \sim -20$ mm.

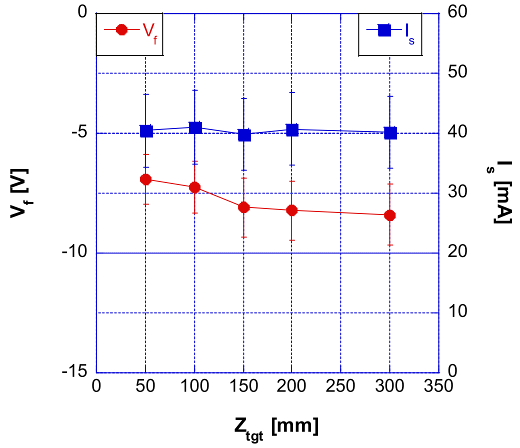

Fig. 10 Floating potential V_f and ion saturation current I_s against Z_{tgt}.

Strong fluctuations are seen at frequencies of 1 - 5 kHz and 15 - 20 kHz in the plasma center. Unfortunately, reflectometry was unable to detect these strong higher frequency oscillations. Instead, the plasma emission measurement system might be used to gauge this. These fluc-

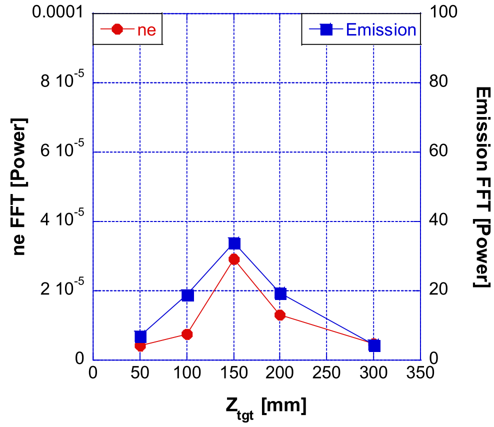

Fig. 11 Fluctuation intensities of electron density and plasma emissions axial dependences of fluctuation frequency of 2.5 - 5.5 kHz.

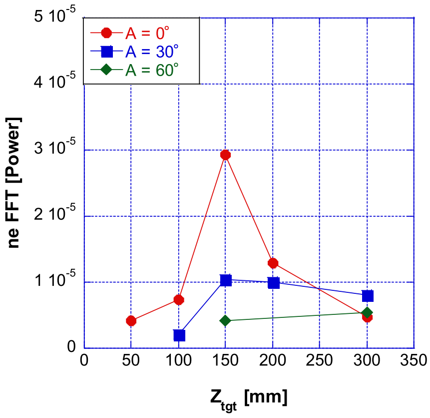

Fig. 12 Electron density fluctuation axial profiles with changing target plate tilt angle.

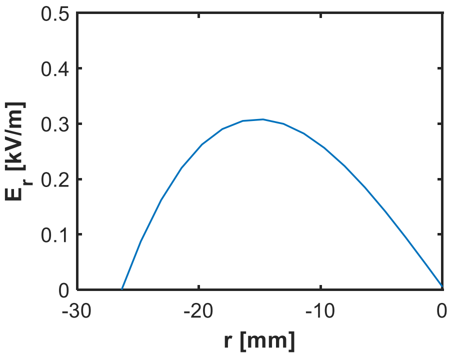

Fig. 13 Electric field strength E_{r} radial profile.

tuation roots are not clear but it is thought that they are caused by the cross-field transport by the $E_\theta \times B$ drift in the plasma center region, where E_θ is an azimuthal electric field [15]. The contour plot of the radial intensity temporal evolution of the fast-framing camera in Fig. 17 confirms the radial extension of the emission intensity in the plasma

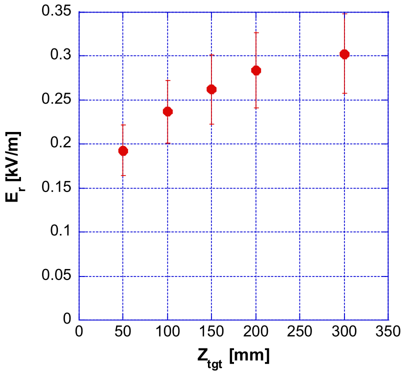

Fig. 14 Electric field strength E_{r} against Z_{tgt}.

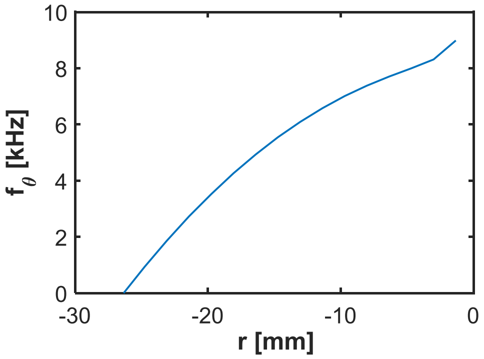

Fig. 15 Calculated frequency against r.

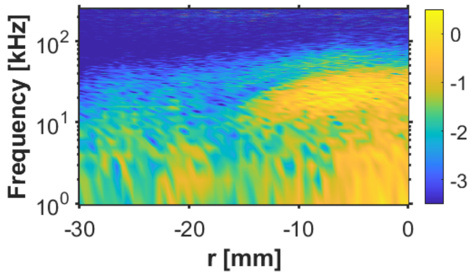

Fig. 16 Fluctuation spectrogram of I_{s} radial profile.

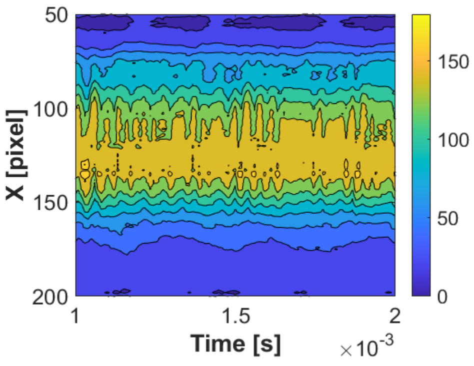

Fig. 17 Contour plot of radial intensity temporal evolution of the fast-framing camera.

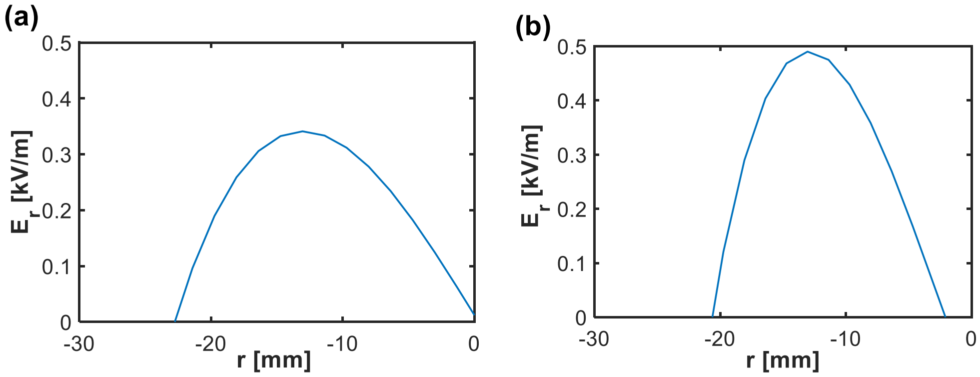

Fig. 18 (a) and (b) show the radial electric fields at A = 30° and 60°, respectively.

center. The spiky radial extensions of emission intensities are indicated, which seems like blob behaviors. It shows the broad frequency fluctuation.

The microwave reflectometry system and fast reciprocating probe were used to quantify the coherent low-frequency electron density fluctuations in the periphery area. The electron density and/or the recombined neutral helium atom fluctuations caused the emission fluctuations that were observed by both the fast-framing camera and PD. The rate coefficient for the recombination process, including the radiative recombination and three-body recombination, at $n_e \sim 2.7 \times 10^{20}\,\mathrm{m}^{-3}$ and $T_e \sim 0.5\,\mathrm{eV}$ is approximately $3 \times 10^{-17}\,\mathrm{m}^3/\mathrm{s}$ (from Ref. [21]), and the mean free path of the ions is approximately 0.7 m. In the lower electron temperature zone, the three-body recombination is predominant, $T_e < 2\,\mathrm{eV}$. In the periphery, it was possible to witness the coherent emission fluctuations from neutral helium atoms created by the recombination of ions and electrons.

The fluctuation peak was observed for both the electron density and emissions at $Z_{\mathrm{tgt}} = 150\,\mathrm{mm}$ in Fig. 11. Both the fluctuations in electron density and emissions exhibit the same axial patterns in this plasma condition. In the edge plasma $r < -10\,\mathrm{mm}$, electron temperature and density are less than 0.3 eV and $1\times10^{20}\,\mathrm{m}^{-3}$, respectively. Compared to the plasma core, the recombination rate coefficient is elevated to over $5\times10^{-17}\,\mathrm{m}^3/\mathrm{s}$ [21]. The three-body recombination is dominant in this lower T_e range. At the position $Z_{\mathrm{tgt}} = 150\,\mathrm{mm}$, the plasma parameters of the peripheral region of the plasma were thought to fit as the recombination front in the detached plasma.

As shown in Fig. 12, there are differences in the axial profiles' fluctuation intensities against the target plate tilt angles. The electron temperature and density remain almost the same as that with the tilt angle changes. The connection length from the measuring position to the wall/target is believed to have an impact on the fluctuation characteristics in addition to the recycling particles. Distance between the observing position and the target plate position appears to be thought to affect the coherent fluctuation intensities. When the target plate is tilted, the differences in the Z_{tgt} position at the top and bottom of the plasma column on the target are, respectively, 0 mm, 29 mm, and 87 mm at A = 0°, 30°, and 60° at $Z_{\mathrm{tgt}} = 150\,\mathrm{mm}$. The coherent fluctuation intensity is affected by changes in target position caused by target plate Z_{tgt} position shifting. The electric field E_r radial profiles at A = 30°, and 60°, respectively, are shown in Figs. 18 (a) and (b). The tilt angles affect the radial profiles of electric field strength. The electric field at $r \sim -20\,\mathrm{mm}$ decreases as the tilt angle increases. The coherent low-frequency fluctuation depends on the electric field E_r.

5. Summary

We conducted a fluctuation analysis to examine the effects of the target plate geometry by changing the target plate position from the axial position at the TS system measurement and target plate tilt angle, including the spatial distribution of fluctuations and the effects of the plasma injection angle on the divertor plate, simultaneously, utilizing the fast reciprocating probe, reflectometry system, photodiode emission measuring system, and fast-framing camera system. The target plate's position and tilt angle dependency showed distinct coherent low-frequency fluctuations. This is the first result that clearly distinguishes between the axial profile and tilt angle dependency fluctuation intensities.

Acknowledgments

We greatly thank the Magnum-PSI team for performing fruitful experiments and discussions. This work was partly supported by the PWI international collaboration program and performed with the support and under the auspices of the NIFS Collaboration Research program (NIFS14KUGM086), NIFS/NINS under Young Researchers Supporting Program (UFEX106), and the JSPS KAKENHI (18KK0410, 19K14686).

[1] S.I. Krasheninnikov, A.S. Kukushkin and A.A. Pshenov, Phys. Plasmas **23**, 055602 (2016).
[2] S. Takamura, N. Ohno, D. Nishijima and Y. Uesugi, Plasma

Sources Sci. Technol. **11**, A42 (2002) [DOI: 10.1088/0963-0252/11/3A/306].

[3] N. Ohno, D. Nishijima, S. Takamura, Y. Uesugi, M. Motoyama, N. Hattori, H. Arakawa, N. Ezumi, S. Krasheninnikov, A. Pigarov and U. Wenzel, Nucl. Fusion **41**, 1055 (2001) [DOI: 10.1088/0029-5515/41/8/309].

[4] N. Ohno, Plasma Phys. Control. Fusion **59**, 034007 (2017) [DOI: 10.1088/1361-6587/aa5394].

[5] K. Okazaki, H. Tanaka, N. Ohno, N. Ezumi, Y. Tsuji and S. Kajita, Rev. Sci. Instrum. **83**, 023502 (2012). [DOI: 10.1063/1.3681778].

[6] M. Yoshikawa, H. Van Der Meiden, R. Al, K. Bystrov, J. Vernimmen, J. Kohagura, Y. Shima, X. Wang, M. Ichimura, M. Sakamoto, Y. Nakashima, Plasma Fusion Res. **10**, 1202088 (2015).

[7] M. Yoshikawa, H. Van Der Meiden, R. Al, J. Vernimmen, J. Kohagura, Y. Shima, M. Sakamoto and Y. Nakashima, AIP Adv. **9**, 085225 (2019) [DOI: 10.1063/1.5099648].

[8] K. Takeyama, N. Ohno, M. Yoshikawa, H. Tanaka and S. Kajita, Plasma Fusion Res. **12**, 1202007 (2017) [DOI: 10.1585/pfr.12.1202007].

[9] H. Tanaka, K. Takeyama, M. Yoshikawa, S. Kajita, N. Ohno and Y. Hayashi, Plasma Phys. Control. Fusion **60**, 075013 (2018) [DOI: 10.1088/1361-6587/aac0d8].

[10] N. Ohno, M. Seki, H. Ohshima, H. Tanaka, S. Kajita, Y. Hayashi, H. Natsume, H. Takano, I. Saeki, M. Yoshikawa and H. van der Meiden, Nucl. Mater. Energy **19**, 458 (2019) [DOI: 10.1016/j.nme.2019.03.010].

[11] H. Tanaka, S. Kajita, H. Natsume, I. Saeki and N. Ohno, Plasma Phys. Control. Fusion **62**, 075011 (2020) [DOI: 10.1088/1361-6587/ab8e19].

[12] H. Natsume, H. Tanaka, S. Kajita, M. Yoshikawa, M. Seki, H. Ohshima and N. Ohno, AIP Adv. **9**, 015016 (2019) [DOI: 10.1063/1.5081929].

[13] Y. Hayashi, K. Ješko, H.J. van der Meiden, J.W.M. Vernimmen, T.W. Morgan, N. Ohno, S. Kajita, M. Yoshikawa and S. Masuzaki, Nucl. Fusion **56**, 126006 (2016) [DOI: 10.1088/0029-5515/56/12/126006].

[14] Y. Hayashi, N. Ohno, H. van der Meiden, J. Scholten, S. Kajita, J. van den Berg, R. Perillo, J. Vernimmen and T. Morgan, Plasma Fusion Res. **14**, 1202135 (2019) [DOI: 10.1585/pfr.14.1202135].

[15] H. Tanaka, Y. Hayashi, S. Kajita, H.J. van der Meiden, M. Yoshikawa, J.W.M. Vernimmen, J. Scholten, I. Classen, T.W. Morgan and N. Ohno, Plasma Phys. Control. Fusion **62**, 115021 (2020) [DOI: 10.1088/1361-6587/abb88f].

[16] S. Potzel, M. Wischmeier, M. Bernert, R. Dux, H.W. Müller and A. Scarabosio, Nucl. Fusion **54**, 013001 (2014) [DOI: 10.1088/0029-5515/54/1/013001].

[17] H.J.N. van Eck, T. Abrams, M.A. van den Berg, S. Brons, G.G. van Eden, M.A. Jaworski, R. Kaita, H.J. van der Meiden, T.W. Morgan, M.J. van de Pol, J. Scholten, P.H.M. Smeets, G. De Temmerman, P.C. de Vries and P.A. Zeijlmans van Emmichoven, Fusion Eng. Des. **89**, 2150 (2014) [DOI: 10.1016/j.fusengdes.2014.04.054].

[18] H.J.N. van Eck, G.R.A. Akkermans, S. Alonso van der Westen, D.U.B. Aussems, M. van Berkel, S. Brons, I.G.J. Classen, H.J. van der Meiden, T.W. Morgan, M.J. van de Pol, J. Scholten, J.W.M. Vernimmen, E.G.P. Vos and M.R. de Baar, Fusion Eng. Des. **142**, 26 (2019) [DOI: 10.1016/j.fusengdes.2019.04.020].

[19] H.J. van der Meiden, A.R. Lof, M.A. van den Berg, S. Brons, A.J. Donné, H.J. van Eck, P.M. Koelman, W.R. Koppers, O.G. Kruijt, N.N. Naumenko, T. Oyevaar, P.R. Prins, J. Rapp, J. Scholten, D.C. Schram, P.H. Smeets, G. van der Star, S.N. Tugarinov and P.A. Zeijlmans van Emmichoven, Rev. Sci. Instrum. **83**, 123505 (2012) [DOI: 10.1063/1.4768527].

[20] A.E. Shumack, V.P. Veremiyenko, D.C. Schram, H.J. de Blank, W.J. Goedheer, H.J. van der Meiden, W.A.J. Vijvers, J. Westerhout, N.J. Lopes Cardozo and G.J. van Rooij, Phys. Rev. E **78**, 046405 (2008) [DOI: 10.1103/PhysRevE.78.046405].

[21] H. Tanaka *et al*., Phys. Plasmas **27**, 102505 (2020).